Available online at www.sciencedirect.com
SCIENCE DIRECT®
ELSEVIER
Earth and Planetary Science Letters 214 (2003) 59–74
EPSL
www.elsevier.com/locate/epsl

An experimental and numerical study of the kinetics of harzburgite reactive dissolution with applications to dunite dike formation

Zachary Morgan, Yan Liang *

Department of Geological Sciences, Brown University, Providence, RI 02912, USA

Received 18 September 2002; received in revised form 31 January 2003; accepted 2 July 2003

Abstract

The mechanisms and kinetics of harzburgite reactive dissolution in basaltic liquids were examined using a combined experimental and numerical approach. Dissolution experiments were conducted at 1250–1290°C and 0.6–0.75 GPa using dissolution couples consisting of pre-synthesized rods of alkali basalt and harzburgite in graphite and platinum-lined molybdenum capsules. Reactive dissolution of harzburgite produces a melt-bearing, orthopyroxene-free dunite with a sharp mineralogical front at the dunite–harzburgite interface. The thickness of the dunite layer is proportional to the square root of experimental run time, and its growth rate is limited by the rates of diffusion of major components in the melt. Around the sharp mineralogical front there exists a broad composition boundary layer where major and trace element abundances in the interstitial melt and olivine vary systematically as a function of distance and time. The sharp mineralogical front and the broad composition boundary layer result from a combined effect of orthopyroxene and olivine dissolution at the dunite–harzburgite interface, olivine re-precipitation within the dunite, as well as diffusive exchange between the crystals and the melts. Based on experimental observations a simple model for harzburgite reactive dissolution was developed and used to extrapolate the experimentally measured dissolution rates and concentration profiles to conditions relevant to melt transport under the mid-ocean ridge. Model calculations demonstrate that diffusive dissolution alone is incapable of producing dunite dikes wider than a few meters within the time scale of mantle upwelling under the mid-ocean ridge. Prevalent melt percolation, hence large melt–rock ratios, is required in the formation of large dunite channels in the mantle. The composition of the reacting melt is of particular importance in determining the composition gradients in olivine across the dunite–harzburgite interface. By adjusting the reacting melt compositions we were able to produce concentration profiles broadly similar to those observed in our experiments as well as those reported across the dunite–harzburgite sharp contacts in the mantle sections of ophiolites and peridotite massifs around the world.
© 2003 Elsevier B.V. All rights reserved.

Keywords: reactive dissolution; harzburgite; dunite; ophiolite; kinetics; melt transport; moving boundary

1. Introduction

It is generally believed that dissolution of harzburgite plays an important role in melt transport beneath mid-ocean ridges. Preferential dissolution

* Corresponding author. Tel.: +1-401-863-9477; Fax: +1-401-863-2058.
E-mail addresses: zachary_t_morgan@brown.edu (Z. Morgan), yan_liang@brown.edu (Y. Liang).

0012-821X/03/$ – see front matter © 2003 Elsevier B.V. All rights reserved.
doi:10.1016/S0012-821X(03)00375-3

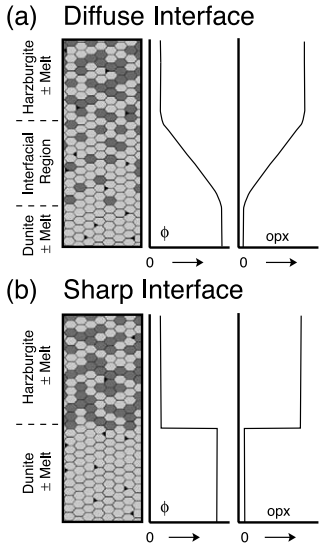


Fig. 1. Schematic representations of a diffuse interface (a) and a sharp interface (b) between dunite and harzburgite. Melt fraction (ϕ) and orthopyroxene (opx) abundance decrease gradually across a diffuse interface. Diffuse interfaces between dunite and harzburgite have been observed in the Semail ophiolite [7], Josephine peridotite [3], Bay of Islands ophiolite [8,16], and the Iwanaidake peridotite [9]. Sharp interfaces have been observed in the Trinity peridotite [10], Semail ophiolite [7], Horoman peridotite complex [11], Josephine peridotite [3], Troodos massif [12], Bay of Islands ophiolite [8,16], and the Iwanaidake peridotite [9].

of orthopyroxene and precipitation of olivine as olivine normative basalt percolates through a harzburgite matrix results in an increase in local melt porosity and matrix permeability, which accelerates melt flow and harzburgite dissolution ([1] and references therein). Such positive feedbacks between dissolution and flow result in reactive infiltration instability [2–5]. Localized high-porosity dunite channels or conduits produced by harzburgite reactive dissolution allow melt to segregate efficiently from its source region while preserving its deep geochemical signatures ([1] and references therein).

Field and petrologic observations of harzburgite-hosted dunite dikes in the mantle sections of ophiolites and other peridotite massifs indicate two types of interfaces between dunite and harzburgite: diffuse interface and sharp interface (Fig. 1a,b). The orthopyroxene abundance drops abruptly to zero across a sharp dunite–harzburgite interface (Fig. 1b), but decreases gradually (though not necessarily smoothly) from harzburgite to dunite in a diffuse interface (Fig. 1a). Both sharp and diffuse interfaces between the harzburgite and dunite have been observed in the mantle section of ophiolites and peridotite massifs, though the sharp interfaces appear to be more abundant (for a detailed list of occurrences see the caption to Fig. 1). Although the exact origins of the sharp and diffuse interfaces are not known, a sharp planar interface can transform into a diffuse interface when the former becomes morphologically unstable [6]. In the sharp interface limit, the dunite–harzburgite transformation is a moving boundary problem that, to our knowledge, has not been examined in the geological literature before. One of the primary purposes of this study is to use harzburgite dissolution experiments and numerical calculations to understand the mineralogical and geochemical consequences of a sharp interface during harzburgite reactive dissolution. The diffuse interface will be the subject of future studies (also see [6]).

At pressures below olivine and orthopyroxene multi-saturation, orthopyroxene dissolves incongruently into basaltic liquids, producing olivine and a silica-enriched melt. Kelemen [13] found that the orthopyroxene dissolution reaction is approximately isenthalpic and results in a slight increase in melt fraction. Asimow and Stolper [14] examined the thermodynamics of mantle–melt interaction using a steady-state transport model and the MELTS program [15]. According to Asimow and Stolper [14] reaction between basalt and lherzolite would first result in a clinopyroxene-free harzburgite and then an orthopyroxene-free dunite with increasing melt fraction. The thermodynamic analyses [13,14] imply a gradual decrease in orthopyroxene abundance as one travels from harzburgite into dunite, i.e. a diffuse interface. It is not known how the thermodynamic-based mechanisms can result in a sharp interface between the harzburgite and the dunite.

Perhaps one of the most interesting petrologic and geochemical observations of dunite and harzburgite from the mantle sections of ophiolites is the presence of composition gradients in major,

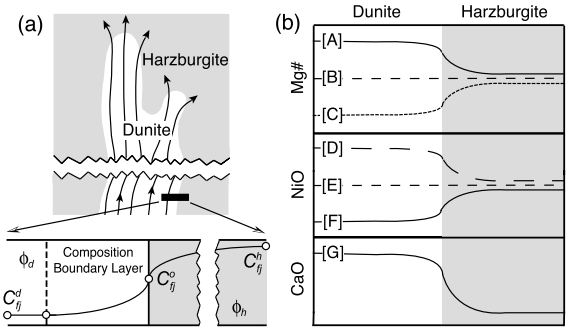


Fig. 2. Schematic representations of a dunite channel in a harzburgite host (a) and observed concentration gradients in the vicinity of a dunite–harzburgite sharp interface (b). Computation domain used in the one-dimensional calculations in Section 4.2 is shown in the lower half of panel (a). The streamlines within the dunite channel illustrate that the predominant melt flow is parallel to the dunite–harzburgite contact, except at the tips of the propagating channel, where the melt flow is normal or oblique to the dunite–harzburgite interface (after Lichtner [17]). Sources of data for panel (b) include: Trinity peridotite ([10], lines [A], [E], [G]), Horoman peridotite ([11], lines [C], [F]), Iwanaidake peridotite ([9], lines [A], [B], [E], [F]), and the Bay of Islands ophiolite ([16], lines [A], [B], [D]–[G]).

minor and trace elements across the contacts between dunite and harzburgite [9–11,16]. Fig. 2b summarizes the observed relative variations in Mg#, NiO, and CaO abundance in olivine in the vicinity of sharp dunite–harzburgite contacts in several ophiolites and peridotite massifs [9–11,16]. Explanations for the observed compositional trends include different degrees of (hydrous) partial melting, and/or various extents of melt–rock reaction. As will be shown in this study, the composition of the through-going melt within the dunite channel is likely to play an important role in determining the elemental abundance and composition gradients in olivine across the sharp interface between dunite and harzburgite.

The presence of concentration gradients in olivine across the dunite–harzburgite contacts suggests that kinetics is likely to play an important role in the harzburgite–dunite transformation. Laboratory crystal dissolution studies indicate that orthopyroxene dissolves faster than olivine in melts of basaltic composition [18–24]. By placing powders of a high-magnesium basalt into a harzburgite crucible at 1200–1250°C and 1 atm for 2 h, Fisk [25] noted that the reacted melt is strongly enriched in SiO_2 (56 wt%), Na_2O (2–3%) and K_2O ($\sim$0.2%), characteristic of high-magnesium andesites or boninites. Lundstrom [26] conducted a set of peridotite–basanite infiltration experiments at 1300°C and 0.9 GPa. Silica- and alkali-enrichment and very fast Na diffusive infiltration were also observed in his study. By juxtaposing powders of H_2O-bearing olivine tholeiite against harzburgite at 1050–1150°C and 0.5 GPa, Kelemen et al. [27] reported several interesting features of harzburgite dissolution, including the characteristic zoning and systematic variations of olivine in the reaction zone. However, because of the powder against powder setup, extensive melt infiltration was likely to take place in their experiments, which would prevent any reliable measurement of the dissolution rate. By juxtaposing disks of pre-synthesized harzburgite against pre-synthesized alkali basalt in a nickel capsule at 1250°C and 0.3 GPa for 6 and 12 h, Daines and Kohlstedt [28] observed two important features of harzburgite dissolution: the presence of an olivine+melt reactive boundary layer between the harzburgite and the alkali basalt, and the development of thin elongated olivine+melt fingers in the harzburgite in the longer-duration runs (12 h). Daines and Kohlstedt [28] attributed the latter to the development of dissolution and flow-induced reactive infiltration instability similar to the mechanism proposed by Ortoleva et al. [2]. No detailed chemical analyses of the experimental products were reported, however.

In two recent numerical and theoretical studies of the grain-scale kinetics of crystal dissolution in molten and partially molten systems, Liang [29,30] has shown that there are two regimes of crystal dissolution: diffusion in melt-limited dissolution (referred to as Regime I dissolution) and diffusion in solid-limited (Regime II) dissolution. Regime I dissolution always over-dissolves, resulting in re-precipitation at later times when the concentration gradients in the local melt pockets become negligible. Liang [29,30] speculated that disequilibrium transformation of a harzburgite into a dunite would produce a sharp mineralogi-

cal front advancing at a velocity rate-limited by the slowest major diffusing species in the melt. Trailing behind the mineralogical front was a broad concentration boundary layer formed by Regime II re-precipitation.

In this paper we present results from an experimental and numerical study of harzburgite dissolution in basaltic liquids. The primary purpose of this study is to characterize the petrologic, mineralogical, and geochemical systematics of harzburgite dissolution. An understanding of the kinetics of harzburgite dissolution will help us to better understand the concentration gradients across the dunite–harzburgite contacts in ophiolites, which in turn will allow us to develop more realistic models for melt transport in the mantle.

2. Experimental methods

Experiments characterizing harzburgite reactive dissolution in an alkali basalt were carried out at 1250–1290°C and 0.6–0.75 GPa using a 19.2 mm piston cylinder apparatus. Dissolution couples consist of pre-synthesized rods of harzburgite juxtaposed against pre-synthesized rods of alkali basalt in graphite- and platinum-lined molybdenum capsules.

Table 1
Starting compositions

Oxide	Alkali basalt[a]	ol[b]	opx[b]	ol[c]
SiO_2	47.10	40.04	54.94	38.85
TiO_2	2.49		0.09	
Al_2O_3	15.04		4.71	
Cr_2O_3			0.45	
FeO[d]	12.50	11.01	6.91	19.22
NiO		0.39		0.05
MnO	0.20	0.18	0.17	0.23
MgO	8.36	47.58	32.07	41.24
CaO	9.95	0.08	0.80	0.33
Na_2O	3.02		0.21	
K_2O	1.00			
P_2O_5	0.36			
Total	100.02	99.28	100.35	99.91
Mg#	54.38	88.51	89.19	79.28

[a] Average of 10 analyses of a sample from the 1800–1801 AD Hualalai lava flow, Hawaii.
[b] Spinel lherzolite from Xalapasco de la Joya, San Luis Potosi, Mexico, sample XDJ-16 of [31].
[c] Average of six analyses of olivine phenocrysts in the alkali basalt from a 0.75 GPa run.
[d] Total FeO.

2.1. Starting materials

The starting materials are an alkali basalt and a harzburgite created by mixing hand-picked optically clean olivine and orthopyroxene (1:1 by weight) from a spinel lherzolite (Table 1). Alkali basalt has a higher reactivity with the synthetic harzburgite than typical mid-ocean ridge basalt (MORB), which allows us to study the dissolution kinetics on the laboratory time scale. The starting materials were ground separately under ethanol in an agate mortar for 20 min to produce a fine powder. The resulting powder was heat-treated (600°C or 800°C) in air for 15 or 1 min to drive off adsorbed water and then stored in a 110°C oven.

2.2. Experiments

The furnace assembly consists of a molybdenum capsule sandwiched between two crushable MgO spacers in a graphite, Pyrex®, and salt sleeve, similar to that used by Liang [32] in his study of quartzite dissolution in molten CaO–Al_2O_3–SiO_2. The molybdenum capsule (6.5 mm OD and 8–10 mm long) was lined with a platinum tube (3–4 mm OD, 2.9–3.8 mm ID) and a graphite inner sleeve (2.8–3.8 mm OD, 2 mm ID). Use of the C–Pt–Mo capsule not only eliminates the sample–container reaction problem but also assures reasonably good geometry of the dissolution couple. To further explore the dissolution mechanism an oxidized nickel capsule was used in one of the dissolution runs described in Section 4.1 (HarzdisNi in Table 2 and Fig. 8). This nickel capsule has dimensions similar to the C–Pt–Mo capsule but without the platinum and graphite inner sleeves.

Approximately cylindrical alkali basalt and harzburgite rods were first synthesized using the C–Pt–Mo or Ni capsule at the same temperatures and pressures as the actual dissolution experiments (4–25 h for the alkali basalt and 6–37 h for the harzburgite). After each synthesis run the capsule was cut in half perpendicular to the cylin-

drical axis using a low-speed diamond-wafering saw. The exposed surface was then polished, and heat-treated at 400°C to remove adsorbed water that may have entered the capsule during the polishing.

Each dissolution couple was made by juxtaposing half of a pre-synthesized alkali basalt rod on top of half of a pre-synthesized harzburgite rod in the C–Pt–Mo or Ni capsule described above. Two platinum bands (0.5–1 mm wide and 9–11 mm long) were placed longitudinally around the dissolution couple. Platinum alloys with molybdenum at the run conditions, which helps to prevent the two halves of the dissolution couple from separating upon decompression. The furnace assembly was then stored at 110°C for at least 12 h. To conduct a dissolution run the charge was first cold-pressurized to a pressure 10–20% higher than the desired run pressure. The temperature was raised to 1000°C at 75°C/min, while keeping the pressure to the prescribed run pressure (hot-piston in). After 1 h of pre-anneal at 1000°C the temperature was then raised to the prescribed run temperature (1250–1290°C) at 150°C/min. At the end of the experiment the run was quenched following the procedure described in [32] and [37]. The quenched capsules were sectioned longitudinally, polished, and mounted for electron microprobe analysis. Table 2 summarizes the experimental conditions. Fig. 3 shows the geometry of a typical dissolution couple and the olivine+melt reactive boundary layer. A slight difference in diameters between the two half cylinders containing the pre-synthesized materials (due to deformation during the synthesis run) results in a small offset at the original rock–melt interface and thus serves as a marker for dissolution distance measurements (Fig. 3).

The temperature was measured using a $W_{97}Re_3$–$W_{75}Re_{25}$ thermocouple and a Eurotherm 818 controller. No pressure correction was applied to the measured emf. Uncertainties in temperature measurements were about 10°C. This is due mainly to the presence of a temperature gradient in the furnace (e.g. [33,34]). The nominal pressure was not corrected for friction because pressure fluctuations during a typical run (~30 MPa) were comparable to the friction correction measured by Ayers et al. [33] for a similar furnace assemblage (~25 MPa).

Table 2
Summary of harzburgite dissolution experiments

Run #	T (°C)	Pressure (GPa)	Duration (h)	Dunite thickness (μm)	Dunite porosity[a] (%)	Harzburgite porosity[b] (%)
Harzdis22	1290	0.6	2.0 (24.4)[c]	142 ± 12[d]	20.7	11.1
Harzdis24	1290	0.6	4.0 (37.4)	180 ± 6	21.2	11.7
Harzdis25	1290	0.6	0.7 (37.4)	70 ± 2	22.9	11.3
Harzdis26	1290	0.6	8.0 (19.5)	190 ± 12	21.7	11.4
Harzdis30	1290	0.6	0.4 (8.6)	61 ± 6	19.6	7.82
Harzdis31	1290	0.6	2.0 (8.6)	145 ± 6	22.9	9.28
HarzdisNi[e]	1290	0.6	2.0 (7.6)	119 ± 5	23.6	7.68
Harzdis28	1250	0.6	2.0 (23.2)	104 ± 7	23.5	14.2
Harzdis32	1251	0.6	0.7 (6.4)	60 ± 4	21.4	9.93
Harzdis36[e]	1260	0.75	4.0 (29.9)	108 ± 17	23.8	8.98
Harzdis37[e]	1260	0.75	8.0 (22.2)	155 ± 12	24.1	10.0
Harzdis38[e]	1260	0.75	4.0 (22.2)	92 ± 15	22.5	7.41
Harzsyn7	1290	0.6	0.0 (12)	0	NA	12.6

[a] Volume fraction of melt in the dunite, relative uncertainty (1σ) is 1.4%.
[b] Relative uncertainty (1σ) is 2.4%.
[c] Numbers in parentheses are duration of harzburgite synthesis run.
[d] One standard deviation estimated from 10 measurements around the central portion of a given charge.
[e] Olivine phenocrysts present in the alkali basalt.

2.3. Microprobe analysis

Chemical analyses were conducted on a Cameca Cambax or a Cameca SX100 electron microprobe at Brown University. Backscattered electron (BSE) images (Fig. 3), X-ray concentration maps (Fig. 8), and concentrations in olivine and orthopyroxene (Figs. 6 and 7) were collected using the Cameca SX100 electron microprobe. Concentration profiles in the melt (Fig. 5) were obtained using the Cameca Cambax electron microprobe. An accelerating voltage of 15 kV was used for both glass and mineral analyses. Beam currents of 10–15 nA and beam diameters of 15–20 μm were used in the glass analyses. Counting times were 10 s for each peak and background position. A focused beam (15–20 nA) was used in the olivine and orthopyroxene analyses. The counting times were 30 s for Ni and Ca, 20 s for Si and Mg, and 10 s for Fe and Mn. Natural glass and mineral standards were used and the PAP correction was employed.

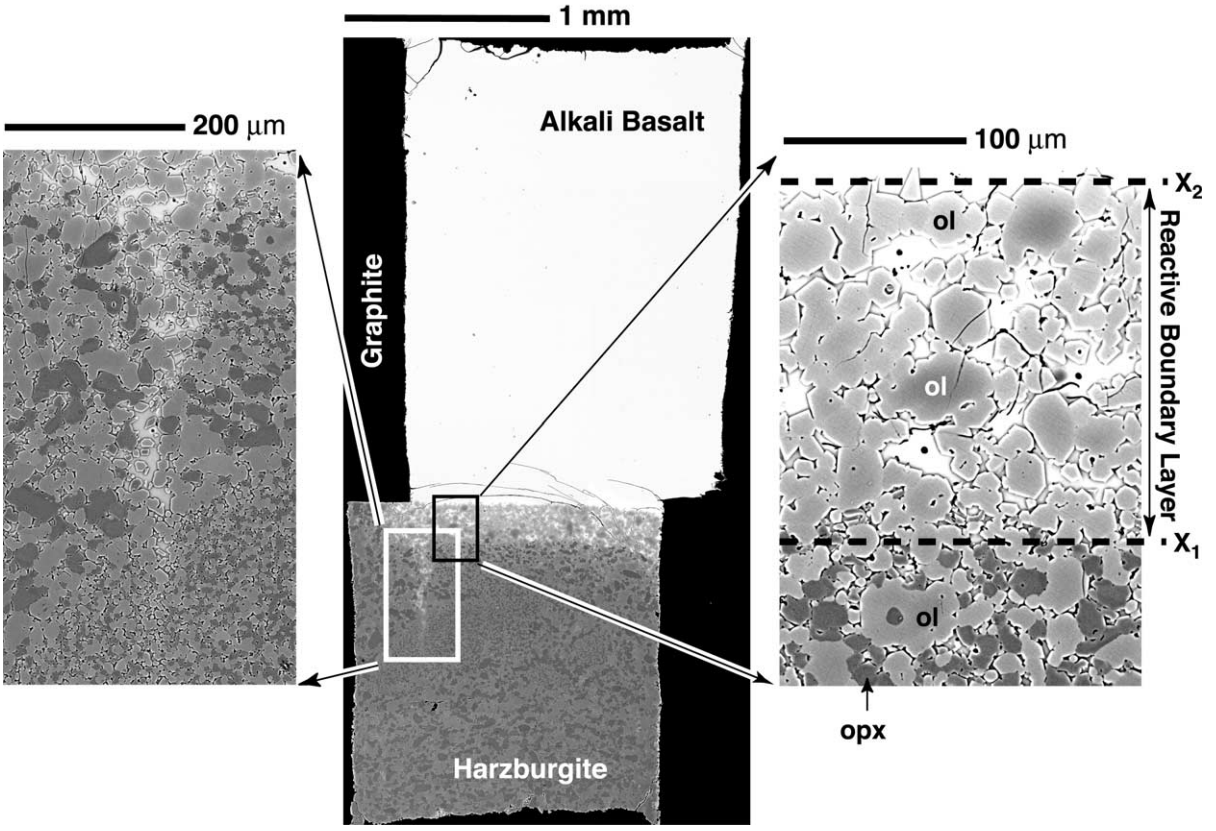


Fig. 3. BSE images of experimental charge Harzdis24 (1290°C, 0.6 GPa, and 4 h). Images include the complete experimental charge (center), a portion of the reactive boundary layer (right) and a melt vein (left). The offset between the two half-capsules marks the original interface between the alkali basalt and the harzburgite. Dashed lines are used to mark the interfaces between the dunite and alkali basalt (X_2) and the dunite and harzburgite (X_1). The reactive boundary layer thickness is given by X_1–X_2.

2.4. Image analysis

Volume fractions of the minerals and interstitial melt were measured using the point counting technique [35]. BSE images were used to calculate the mineral proportions in the harzburgite. Reflected light images were used to measure the fractions of interstitial melt and the reactive boundary layer thickness (defined as X_1–X_2 in Fig. 3).

3. Results and discussions

A total of 18 dissolution experiments were conducted in the course of this study. Six of the 18 runs suffered from one of the following problems: Fe loss due to leaks in the graphite inner capsule, failure or oxidation of thermal couple, large offset or irregular geometry. These failed runs were excluded from this report.

Each experimental charge consists of three distinct regions: alkali basalt, melt-bearing harzburgite, and an orthopyroxene-free, olivine+melt reactive boundary layer (Fig. 3). For simplicity we will refer to the olivine+melt reactive boundary layer and the melt-bearing harzburgite as dunite and harzburgite, respectively. The alkali basalt is generally free of crystals except for runs conducted at 0.75 GPa, where a few rounded olivines (Mg# = 79, Table 1) were present (Harzdis36 to Harzdis38 in Table 2). The harzburgite contains approximately 50 (vol)% subhedral olivine, 40% orthopyroxene, and 10% interstitial melt (Table 2). The grain size ranges from 5 to 50 μm. The

melt fractions in the harzburgite do not show any significant variations with the run duration, suggesting that most of the interstitial melts were generated during the synthesis runs. This is consistent with a zero time experiment in which the harzburgite has 12.6% interstitial melt (Harzsyn7 in Table 2). As will be shown in Section 4.2, the melt fraction in the harzburgite has only a small effect on the rate of harzburgite dissolution under the conditions explored in this study.

As shown in Fig. 3, the harzburgite and the dunite are separated by a sharp mineralogical interface, i.e. the orthopyroxene abundance drops abruptly from ~40% in the harzburgite to 0 in the dunite. The dunite consists of euhedral to subhedral olivine and 19–24% interstitial melt (Table 2 and Fig. 3). Some of the olivine crystals in the dunite contain small melt inclusions consistent with grain growth/coalescence. Small amounts of dendritic to needle-like olivine (<5 μm in length and $<1\%$ in volume) were observed in the dunite and the harzburgite. These quench crystals overgrow on the surfaces or edges of existing olivine and orthopyroxene.

Thin melt-rich veins surrounded by euhedral olivine crystals were observed in the harzburgite in several runs (e.g. left panel in Fig. 3). (Similar melt veins were also observed in several dissolution experiments of quartzite in molten CaO–Al_2O_3–SiO_2, Liang, unpublished data.) Unlike the reactive fingers reported by Daines and Kohlstedt [28] the occurrence of the melt-rich veins in our dissolution experiments is not correlated with run duration. Instead, they appear to be associated with pre-existing cracks along or near the edges or offsets of the capsule, created when the dissolution couples were cold-pressurized. These melt-rich veins are likely produced by spontaneous melt infiltration along the pre-existing cracks and subsequent local dissolution when the dissolution couples were brought to the run temperature.

3.1. Growth of reactive boundary layer

Fig. 4 displays the measured dunite layer thickness (defined as X_1–X_2 in Fig. 3) as a function of the square root of run time. Growth of the dunite layer is linear in this plot, suggesting diffusion is the dominant mechanism of mass transfer (see Eq. 4,5 below). The lower than expected reactive boundary layer thickness in one of the 8-h runs (Harzdis26) is probably due to one of the following reasons: inter-experimental errors, finite geometry effect, i.e. the diffusing species reaches the end of the capsule containing the alkali basalt and hence reducing the driving force for dissolution (Fig. 5; also see [30]), or a combination of the two. For example, Mg# of the alkali basalt at the far-field in this run is 56, two units higher than its original value (Fig. 5d). The parabolic growth law suggests that melt flow or infiltration is not significant in our dissolution experiments. Also plotted in Fig. 4 are two dunite layer thicknesses by measured Daines and Kohlstedt [28] (open circles), who conducted harzburgite dissolution experiments using similar starting compositions at 1250°C and 0.3 GPa. The differences between our measured dissolution distances and those reported in [28] are likely due to the differences in experimental run conditions.

3.2. Melt compositions

Fig. 5 shows concentration profiles in the alkali basalt and interstitial melt in the dunite as a function of normalized distance for run Harzdis26. For clarity, the spatial relations in the dunite ($x<0$) are expanded by a factor of 10 relative to those in the alkali basalt ($x>0$). Melt compositions in the dunite are controlled by several factors, including orthopyroxene dissolution, diffusive exchange between the interstitial melt and the alkali basalt, as well as olivine precipitation (including quench growth). Although quench modification can also affect the interstitial melt composition, it will not significantly alter the broad trends shown in Fig. 5. (The scatter in the data is likely due to quench modification.) This is further supported by the numerical calculations shown in Section 4.3. Preferential dissolution of orthopyroxene increases the SiO_2 abundance in the interstitial melt at the dunite–harzburgite interface ($10x/t^{1/2}=-15$ in Fig. 5a). The diffusive fluxes of Na_2O and K_2O (and to a lesser extent CaO, FeO, and MgO) are strongly

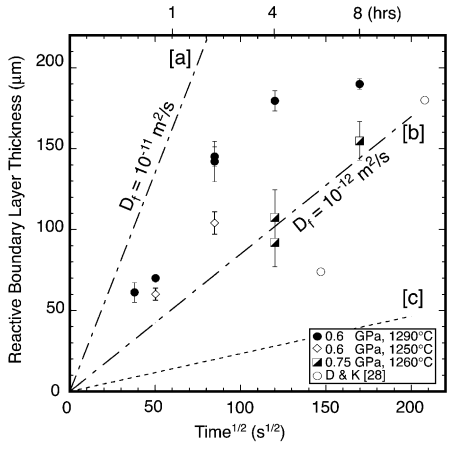


Fig. 4. Plot of measured reactive boundary layer thickness as a function of the square root of time. The two measured data from Daines and Kohlstedt [28] are included for comparison (open circles). Lines [a]–[c] are calculated dunite layer thicknesses using Eq. 3 with diffusion of SiO_2 in the melt as the rate-limiting factor (see Section 4.2 for details). Parameters used in estimates [a] and [b] are: $C^{o}_{fj} = 54$, $C^{d}_{fj} = 47$, $C^{h}_{fj} = 50$, $C^{d}_{sj} = 39.95$, and $C^{h}_{sj} = 47.50$, $\phi_d = 0.20$, $\phi_h = 0.10$. $D_f = 10^{-11}$ m^2/s in [a] and $D_f = 10^{-12}$ m^2/s in [b]. Parameters used in estimate [c] are: $C^{o}_{fj} = 49.5$, $C^{d}_{fj} = 49$, $C^{h}_{fj} = 49$, $C^{d}_{sj} = 40.67$, and $C^{h}_{sj} = 41.65$, $\phi_d = 0.04$, $\phi_h = 0.02$, and $D_f = 10^{-12}$ m^2/s. Geometric relationships of these parameters are defined in Fig. 2a.

coupled to the concentration gradients of SiO_2 in a basaltic melt (e.g. [26,36–38]). Concentrations of the alkali elements increase (also see Fig. 8), whereas the CaO and FeO contents in the melt decrease, towards the dunite–harzburgite interface. Al_2O_3, FeO and TiO_2 are less abundant in the orthopyroxene than in the alkali basalt, so the dissolved orthopyroxene also has a dilution effect.

3.3. Olivine and orthopyroxene compositions

The synthetic harzburgites contain approximately 40% orthopyroxene. Although minor concentration gradients were observed in the outermost layer of orthopyroxene grains, due to partial melting and slow solid-state diffusion, compositions of orthopyroxene in the harzburgite are approximately uniform up to the dunite–harzburgite interface (Fig. 6a).

A majority of the olivine cores in the orthopyroxene-free dunite were pre-existing grains from the harzburgite that experienced dissolution and precipitation. A few olivine dendrites (< 5 μm in length and $< 1\%$ in volume) were observed in the dunite. Quench modification would at most modify the composition of the outermost layer of olivine that was in general excluded in the microprobe analysis. The observed compositional gradients of olivine in the dunite and harzburgite are not significantly affected by quench modification. This is further supported by the numerical calculations shown in Section 4.3 (Fig. 10). Fig. 6 displays the olivine composition as a function of position within the charge Harzdis24. Mg# and NiO in olivine increase and CaO in olivine decreases through the dunite and into the harzburgite. The small bumps with higher (lower) than background NiO (CaO) and Mg# values (Fig. 6b–d, also see composition maps in Fig. 8) reflect the compositional zoning within individual olivine crystals. The presence of compositionally zoned olivine shows that the rate of orthopyroxene dissolution, hence the rate of the dunite growth, is faster than the rate of diffusive re-equilibration between the olivine and interstitial melt and that most of the olivine cores in the dunite existed prior to dissolution. The presence of melt inclu-

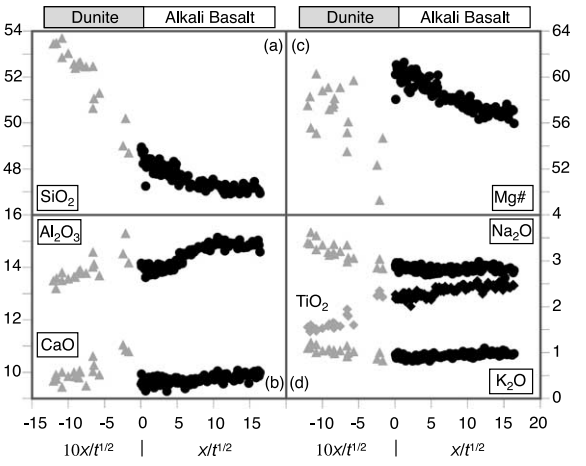


Fig. 5. Plots of measured concentration profiles in the alkali basalt (filled circles, diamonds for TiO_2) and interstitial melt in the dunite (gray triangles, diamonds for TiO_2) as a function of distance normalized by the square root of time (in μm/s$^{1/2}$) for run Harzdis26 (1290°C, 0.6 GPa, 8 h). The positions within the dunite are expanded by a factor of 10 in order to make the data more visible.

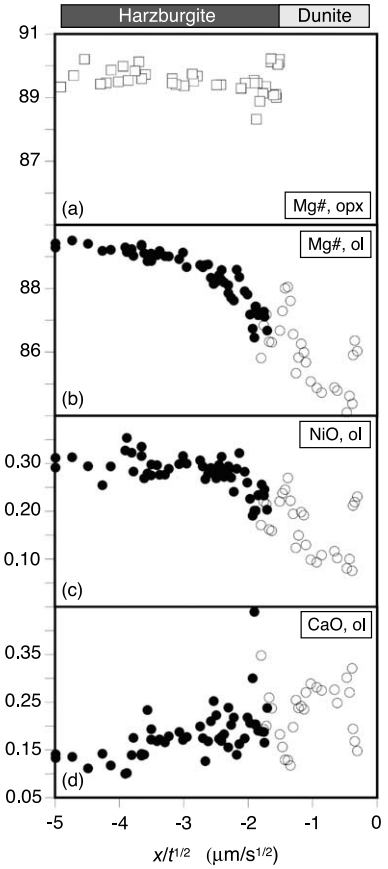


Fig. 6. Plots of measured concentration profiles in olivine and orthopyroxene from the dunite and harzburgite as a function of distance normalized by the square root of time (in $\mu m/s^{1/2}$) for run Harzdis24. The open squares in panel (a) represent measured orthopyroxene compositions in the harzburgite. The open circles in panels (b)–(d) represent measured olivine compositions in the dunite, and the filled circles in panels (b)–(d) are measured olivine compositions in the harzburgite.

sions in the olivine also supports olivine growth in the dunite. The extent of zoning in olivine decreases with the increase of run time, but the overall profile remains the same. Fig. 7 shows that NiO and CaO are strongly correlated with the Mg# of olivine. Similar correlations have been observed across dunite–harzburgite contacts in ophiolites and peridotite massifs [9–11,16]. These correlations will be further examined in Section 4.3.

4. Kinetics of harzburgite reactive dissolution

The dissolution experiments conducted in this study help us to identify several important features of harzburgite dissolution. These include variations in melt composition within the dunite, variations in olivine composition in the dunite and harzburgite, and the sharp mineralogical front separating the orthopyroxene-free dunite and the harzburgite. These systematic variations will be used to constrain the dissolution kinetics.

4.1. Dissolution mechanisms

Both olivine (Mg# = 88.5) and orthopyroxene in the pre-synthesized harzburgite are not in chemical equilibrium with the alkali basalt, even in the 0.75 GPa runs where a few lower-Mg# (~79, Tables 1 and 2) olivine phenocrysts were present in the alkali basalt. Hence both the orthopyroxene and olivine in the harzburgite dissolve or partially dissolve into the alkali basalt. At pressures below olivine+orthopyroxene multi-saturation, orthopyroxene dissolves incongruently into the alkali basalt, resulting in olivine precipitation (e.g. [21,23]). According to the analysis of Liang

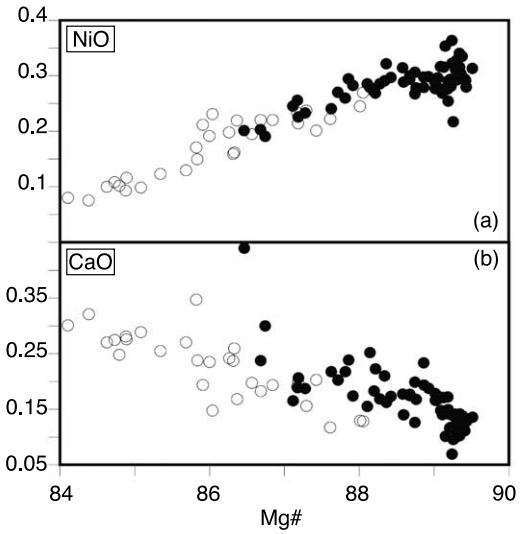


Fig. 7. Correlations between NiO and Mg# in olivine (a) and CaO and Mg# in olivine (b) in the dunite and harzburgite for Harzdis24. The open and filled circles represent olivine compositions in the dunite and the harzburgite, respectively.

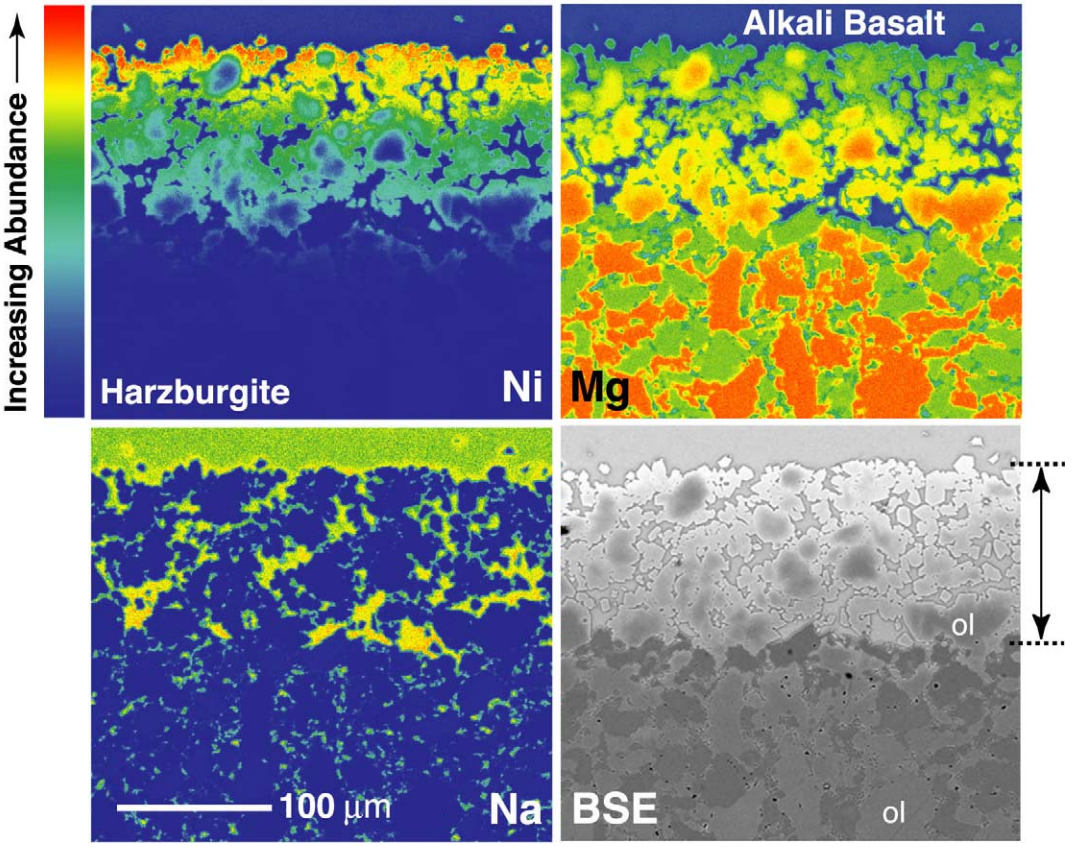


Fig. 8. False-colored X-ray concentration maps of Ni, Mg and Na from a harzburgite dissolution experiment that was conducted using an oxidized nickel capsule (HarzdisNi, 1290°C, 0.6 GPa, 2 h). The X-ray concentration maps were collected using the Cameca SX100 electron microprobe (20 kV accelerating voltage and 50 nA beam current). Blue color in each map represents relatively low concentrations. NiO dissolves into the alkali basalt at the experimental run conditions and re-precipitates as Ni-rich olivine in the reactive boundary layer. The Na concentration map highlights the melt distribution within the dunite and the harzburgite. Note the high Na concentrations at/near the dunite–harzburgite interface. For reference a BSE image of approximately the same area is also shown.

[30], disequilibrium between the alkali basalt and the original olivine will first result in diffusion in melt-limited olivine dissolution followed by diffusion in solid-limited olivine re-precipitation.

This dissolution and re-precipitation process can be checked by a crude mass balance calculation using the composition of orthopyroxene in the harzburgite, average compositions of olivine and interstitial melt in the dunite, and the starting alkali basalt. For example, dissolution of 1 g of orthopyroxene in the harzburgite will precipitate 0.63 g of new olivine, increasing the melt by 2.4 g. This is consistent with the analysis of Kelemen [13].

The dissolution and re-precipitation process was also magnified in a harzburgite dissolution experiment using an oxidized nickel capsule that does not have the platinum and graphite inner sleeves (run HarzdisNi in Table 2). Because NiO dissolves into the alkali basalt at the run condition (1290°C and 0.6 GPa), we were able to use Ni as a chemical tracer to study the dissolution process. Fig. 8 shows false-colored X-ray concentration maps of Ni, Mg, and Na from an area around the dissolution fronts in this charge. The alkali basalt contains 1.5% dissolved NiO, the olivine in the harzburgite contains 0.39% NiO, whereas the olivine crystals in the dunite have a

maximum of 13.5% NiO (blue through red in the Ni map in Fig. 8). Two forms of the precipitated or re-precipitated olivine are observed in the dunite: small euhedral crystals that are absent in the harzburgite (BSE image in Fig. 8), and growing rims around large pre-existing olivine (Ni and Mg maps in Fig. 8). (Practically identical features were also observed in a series of harzburgite dissolution experiments using a hydrous basaltic andesite in an oxidized nickel capsule [39].) It can be checked that diffusive exchange between olivine in the dunite and the interstitial melt *alone* cannot account for the high NiO abundance in the olivine within the dunite, especially for olivine crystals having a size larger than 12 μm (based on a diffusivity of 10^{-15} m^2/s for NiO in olivine [40] and a time of 2 h).

Hence both olivine and orthopyroxene dissolve or partially dissolve into the basaltic liquid. The dissolved olivine components mix diffusively with the surrounding melt and re-precipitate around, or grow on the surface of, partially reacted olivine in the reactive boundary layer forming chemically zoned, Ni-rich olivine. This dissolution and re-precipitation mechanism is consistent with the alkali basalt–harzburgite dissolution experiments reported in Section 3 and the theoretical study of Liang [30].

4.2. Dissolution rate

The growth rate of the reactive boundary layer is determined by the net mass flux across the dunite–harzburgite interface. In the absence of matrix deformation and melt flow, continuity of the mass flux of a component (j, say) across the dunite–harzburgite interface takes the form:

$$\phi_d D_{fj}\left.\frac{\partial C^d_{fj}}{\partial x}\right|_{Xb-} + [\phi_d C^o_{fj} + (1-\phi_d)C^d_{sj}]V = \phi_h D_{fj}\left.\frac{\partial C^h_{fj}}{\partial x}\right|_{Xb+} + [\phi_h C^o_{fj} + (1-\phi_h)C^h_{sj}]V \quad (1)$$

where ϕ is the melt porosity, D_{fj} and C_{fj} are the diffusion coefficient and concentration of component j in the melt, respectively, C_{sj} is the bulk solid composition of j, superscript and subscript 'd' and 'h' refer to properties in the melt-bearing dunite and harzburgite, respectively, C^o_{fj} is the melt composition at the dunite–harzburgite interface advancing at the velocity V. The partial derivatives in Eq. 1 are evaluated at the dunite ($x = Xb-$) and harzburgite ($x = Xb+$) sides of the interface. Eq. 1 is valid for a sharp interface across which the melt and mineral fractions change abruptly (Fig. 1b) and the density differences between the melt and solids are small. To a good approximation the concentration gradients in Eq. 1 can be written as:

$$\left.\frac{\partial C^d_{fj}}{\partial x}\right|_{Xb-} \approx \frac{C^o_{fj} - C^d_{fj}}{Xb} \quad (2a)$$

$$\left.\frac{\partial C^h_{fj}}{\partial x}\right|_{Xb+} \approx \frac{C^h_{fj} - C^o_{fj}}{Xb} \quad (2b)$$

where C^d_{fj} and C^h_{fj} are the far-field melt compositions (Fig. 2a). The linear concentration gradient is consistent with our measured and calculated concentration profiles in the interstitial melt and olivines in the vicinity of the dunite–harzburgite interface (e.g. Figs. 5, 6 and 10a,d). If the porosity and the melt and solid compositions at the interface are independent of time (t), Eqs. 1–2b can be integrated for the dissolution distance, Xb:

$$Xb = L + \sqrt{\frac{2[\phi_h(C^h_{fj} - C^o_{fj}) - \phi_d(C^o_{fj} - C^d_{fj})]D_{fj}t}{[\phi_d C^o_{fj} + (1-\phi_d)C^d_{sj}] - [\phi_h C^o_{fj} + (1-\phi_h)C^h_{sj}]}} \quad (3)$$

where L is the initial half-width of the dunite channel. Eq. 3 can be used to extrapolate our laboratory-measured harzburgite dissolution rates for the highly reactive alkali basalt to less reactive but more relevant MORB compositions.

Fig. 2a shows a schematic representation of the melt compositions across a dunite–harzburgite contact that will be used to relate our model calculations to the dunite channels found in the field. To further simplify our calculations we take an effective binary approach and assume that SiO_2 is the rate-limiting component. This is a reasonable assumption since SiO_2 is the slowest major diffusing component in the silicate melt (e.g. [36]). It has been shown that the rate of crystal dissolution is dominated by the rate of the slowest

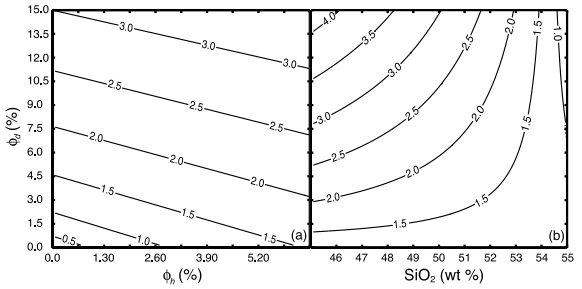


Fig. 9. Contour plots of the reactive boundary layer thickness calculated using Eq. 3 (in mm) and a time $t=1$ yr as a function of the melt porosities in the dunite (ϕ_d) and harzburgite (ϕ_h) (a) and the SiO_2 content in the through-going melt in the dunite channel (b). Parameters used in panel (a) are: $C^o_{fj}=54$, $C^d_{fj}=49$, $C^h_{fj}=50$, $C^d_{sj}=40.67$, $C^h_{sj}=47.50$, and $D_f=10^{-12}$ m^2/s. Parameters used in panel (b) are: $C^o_{fj}=54$, $C^h_{fj}=50$, $\phi_h=4\%$ $C^d_{sj}=44.82$, $C^h_{sj}=47.50$, and $D_f=10^{-12}$ m^2/s. See Fig. 2a for a definition of the symbols.

major diffusing species in the melt in a multi-component system [30,32,41].

Fig. 4 shows three calculated dissolution distances using Eq. 3 with SiO_2 as the rate-limiting component. Estimates [a] and [b] correspond to the starting compositions similar to our dissolution experiments, whereas [c] corresponds to conditions prevalent beneath a mid-ocean ridge. The effective binary diffusion coefficient of SiO_2 in the interface melt has not been measured in this study, but is likely in the range of 10^{-11}–10^{-12} m^2/s at 1260–1290°C, based on previous diffusion studies (e.g. [36,42]). As shown in Fig. 4, good agreement between our measured and calculated dissolution distances was found. Using estimate [c] we can obtain the growth rate of a well-developed dunite dike where lateral advection across the dunite–harzburgite interface is negligible (area near the rectangular bar in Fig. 2a). For example, the width of an existing dunite channel would increase by 0.003 m after 1 yr and 0.84 m after 75 ka. These estimates are likely to be lower bounds because melt flow across the dunite–harzburgite interface is not considered. Nevertheless, our order of magnitude calculations show that pure diffusive dissolution alone is incapable of producing dunite channels wider than a few meters within the time scale of mantle upwelling under the mid-ocean ridge. Prevalent melt flow (i.e. large melt–rock ratios) must be responsible for the formation of larger dunite dikes observed in the ophiolites. This is consistent with the thermodynamic analyses of Kelemen [13] and Asimow and Stolper [14], who argued for large melt–rock ratios in the formation of dunite from harzburgite.

Fig. 9 compares the roles of melt porosity and through-going melt composition on the rate of harzburgite dissolution. The dissolution rate increases with the increase of the melt fractions, with the melt fraction in the dunite playing a

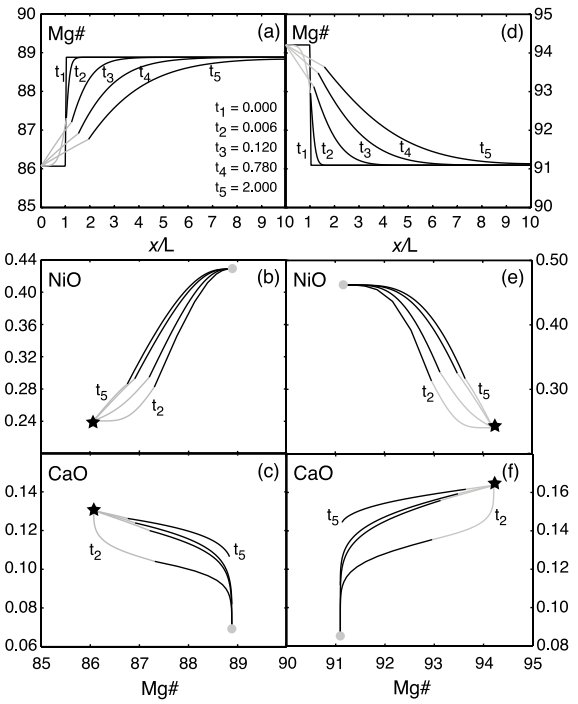


Fig. 10. Calculated concentration profiles and elemental correlations in olivine across a dunite–harzburgite sharp dissolution front for two prescribed boundary conditions (details listed in Table 3) and five selected times. The gray curves correspond to olivine compositions in the composition boundary layer in the dunite and the black lines represent the olivine compositions in the harzburgite. Variations of the Mg# in olivine as a function of position are shown in panels (a) and (d). Correlations between NiO (wt%) and Mg# and CaO (wt%) and Mg# in olivine are shown in panels (b), (c), (e) and (f). The gray circles mark the initial harzburgite composition and the black stars are the initial dunite composition. The distance (x) is scaled by the initial composition boundary layer thickness (L) in the dunite. Assuming the initial length (L) to be 1 m, the actual time will be 2.7×10^5 yr multiplied by the non-dimensional times listed in panel (a).

more prominent role than the melt fraction in the harzburgite (Fig. 9a). This is expected, as the dissolution reaction depends on the amount of harzburgite exposed to the through-going basalt. Fig. 9b compares the relative importance of the melt fraction in the dunite and the reacting melt composition. For the small porosities ($\phi_d < 3\%$) pertinent to melt transport under the mid-ocean ridge (e.g. [1,43]), the dissolution rate depends strongly on the melt fraction in the dunite and is not very sensitive to the through-going melt composition. As the porosity increases, the reacting melt composition becomes more important.

4.3. *Effects of through-going melt composition on harzburgite reactive dissolution*

Some differences between our laboratory results and the field observations (e.g. [9–11,16]) are related to differences in the melt composition involved in harzburgite dissolution. This can be illustrated using a simple diffusive dissolution model that treats the harzburgite dissolution as a moving boundary problem and calculates the olivine compositions in the composition boundary layer and the harzburgite as a function of time for a variety of basaltic compositions. For simplicity and without loss of generality we consider a one-dimensional, periodically distributed olivine+melt dunite channel of initial width of $2L$ in a harzburgite host of initial unit width of $18L$ (Fig. 2a). To focus on the moving boundary aspect of harzburgite dissolution we assume that the interstitial melt is in instantaneous chemical equilibrium with its host rock. Diffusion equations for a major component j in the interstitial melt in the dunite and harzburgite have the usual form (e.g. [43]):

$$\frac{\partial C_{fj}^{d,h}}{\partial t} = D_j^{d,h}\frac{\partial^2 C_{fj}^{d,h}}{\partial x^2} \qquad (4,5)$$

where $C_{fj}^{d,h} = (C_{fj}^{d}, C_{fj}^{h})$, and $D_j^{d,h} = (D_j^{d}, D_j^{h})$ are the effective diffusion coefficients of j in the melt, given by:

$$D_j^{d,h} = \frac{\phi_{d,h} D_{fj}}{\phi_{d,h} + (1-\phi_{d,h})K_j^{d,h}} \qquad (6)$$

K_j is the bulk solid–melt equilibrium partition coefficient. Also for simplicity we assume constant melt porosities and neglect the effects of matrix deformation and melt flow. These effects, as well as finite crystal–melt exchange rates, will be considered in the future. The boundary conditions are a constant composition at the far-side of the dunite composition boundary layer (Fig. 2a, and also $x = 0$ in Fig. 10a,d) and non-flux at the center of the harzburgite ($x/L = 10$ in Fig. 10a,d). The boundary condition at the dunite–harzburgite sharp interface is given by Eq. 1.

Both the interface melt composition C_{fj}^{o} and the dunite–harzburgite interface velocity V are not known a priori and can be determined from Eq. 1 and the harzburgite liquidus in a manner similar to the multi-component crystal dissolution problems examined by Liang [29,30,32]. Since the harzburgite liquidus is not well known and our main purpose here is to illustrate some of the essential features of harzburgite dissolution, we will again take the effective binary approach by assuming SiO_2 as the rate-limiting component. Under these limiting conditions, the SiO_2 abundance in the interface melt remains constant so that we can use Eq. 1 to calculate V. Given V, we can then use Eq. 1 to calculate interface compositions for the other components in the melt and the solid matrices (e.g. MgO, FeO, NiO and CaO). Given the crystal and melt compositions at the interface, Eqs. 4 and 5 were integrated numerically using a variable-grid finite-difference method [44–46] on the computational domain shown in Fig. 2a.

To relate the results of our laboratory experiments to the field observations [9–11,16], several cases with different initial compositions were examined. Parameters used in two sets of calculations are listed in Table 3. Case 1 (Fig. 10a–c) uses conditions similar to our harzburgite dissolution experiments, i.e. an FeO-rich melt (Mg# = 65) reacting with a harzburgite (Mg# = 89). The dunite–harzburgite interface moves to the right as orthopyroxene dissolves into the interstitial melt while olivine re-precipitates. Fig. 10a shows the Mg# of olivine at five selected times. After an initial transient time ($t < 0.1$ units of non-dimensional time; see legend to Fig. 10 for details) concentration profiles in the dunite reach a quasi-steady state and the concentration gradients are

Table 3
Parameters used in numerical modeling[a]

	Compositions					$-\log D_f$ (m^2 s^{-1})	K_j^d ol/liq	K_j^h (ol+opx)/liq
	C_{fj}^d	C_{fj}^h	C_{fj}^o	C_{sj}^d	C_{sj}^h			
Case 1								
SiO_2	47.00	50.00	50.00	39.95	47.50	12	0.85	0.95
NiO	0.02	0.04	0.04	0.24	0.26	11	12.02	6.59
CaO	9.95	5.27	11.50	0.30	0.42	11	0.03	0.08
MgO	10.50	12.07	10.50	45.36	39.83	11	4.32	3.30
FeO	10.00	8.88	9.00	13.10	8.97	11	1.31	1.01
Phase proportions in harzburgite:				45% ol+45% opx+10% melt				
Phase proportions in dunite:				80% ol+20% melt				
Case 2								
SiO_2	49.00	49.00	49.50	40.67	40.18	12	0.83	0.82
NiO	0.02	0.04	0.04	0.24	0.35	11	12.02	8.74
CaO	12.50	6.79	11.50	0.38	0.34	11	0.03	0.05
MgO	12.33	11.3	11.00	53.27	41.36	11	4.32	3.66
FeO	4.46	6.5	6.00	5.84	7.22	11	1.31	1.11
Phase proportions in harzburgite:				78% ol+18% opx+4% melt				
Phase proportions in dunite:				90% ol+10% melt				

[a] ol = olivine; liq = liquid; opx = orthopyroxene; in Case 1 solid/melt partition coefficients (K_j) for MgO, FeO, and CaO are from [47], and NiO is from [48]; in Case 2 K_j for MgO, FeO are from [49], CaO from [50], and NiO from [51]. For convenience of numerical calculations a constant partition coefficient is introduced for SiO_2.

approximately linear in the vicinity of the interface. However, the interface location, as well as the melt and solid compositions at the dunite–harzburgite interface, continues to evolve as a function of time. The discontinuous slopes between the dunite and harzburgite in Fig. 10 are due to differences in the effective diffusion coefficient between the two (Eq. 6). By the time $t = 2$, diffusion of FeO and CaO has reached the center of the harzburgite column ($x/L = 10$). The initial conditions chosen for Case 1 result in a lower NiO content in the dunite than in the harzburgite (Fig. 10b). Hence NiO is positively correlated with the Mg# of olivine. The opposite can be seen for CaO in olivine (Fig. 10c). These results are in good agreement with our harzburgite dissolution experiments (Figs. 6 and 7). Qualitatively they also agree with the general trends observed by Takahashi [11] across the dunite–harzburgite contact in the Horoman peridotite complex (Fig. 2b).

Fig. 10d–f shows the results of a numerical experiment with conditions similar to several field observations [9,10,16]. In this example, a high-Mg# melt (Mg# = 83) reacts with the harzburgite (Mg# = 91, Fig. 10d). Similar to Case 1, by the time $t = 0.1$ diffusion in the dunite composition boundary layer reaches a quasi-steady state. As shown in Fig. 10e, the NiO and Mg# in the olivine are inversely correlated, in contrast to the case shown in Fig. 10b. The negative (positive) correlation between the NiO (CaO) content in olivine and Mg# of olivine is very similar to those observed in the peridotite samples reported by Quick [10], Kubo [9] and Suhr et al. [16] (Fig. 2b). Clearly, composition of the through-going melt has played a very important role in determining the elemental correlations observed across a dunite–harzburgite contact in ophiolites.

We hope the results presented here will stimulate more systematic and detailed studies of the compositional and mineralogical variations across the dunite–harzburgite boundary in ophiolites and peridotite massifs around the world. It is in the vicinity of a dunite–harzburgite contact that one is most likely to find evidence of reactive dissolution. With more realistic models that include melt flow, matrix compaction, finite crystal–melt exchange rate, proper phase diagram, and subsolidus re-equilibration, it is possible to infer the through-going melt compositions as well as the time scales of melt migration through the dunite

channels from detailed compositional traverses across the dunite–harzburgite interface. With a better understanding of the kinetics of harzburgite reactive dissolution, it is also possible to establish the relationship between the sharp and diffuse reaction fronts. As shown elsewhere, a diffuse mineralogical interface can be produced during reactive dissolution when the sharp dunite–harzburgite interface becomes morphologically unstable and chemical diffusion in the infiltrating melt is destabilizing [6].

Acknowledgements

We wish to thank Paul Hess and Alyssa Beck for comments and suggestions to earlier versions of this paper. Constructive reviews by Hugh O'Neill, an anonymous reviewer, and the editor Bernard Wood helped to clarify this manuscript and are greatly appreciated. This work was supported by NSF Grants EAR-9903020 and EAR-0208141.*[BW]*

References

[1] P.B. Kelemen, G. Hirth, N. Shimizu, M. Spiegelman, H.J.B. Dick, A review of melt migration processes in the adiabatically upwelling mantle beneath oceanic spreading ridges, Philos. Trans. R. Soc. Lond. A 355 (1997) 283–318.

[2] P. Ortoleva, E. Merino, C. Moore, J. Chadam, Geochemical self-organization, I, reaction-transport feedbacks, Am. J. Sci. 287 (1987) 979–1007.

[3] P.B. Kelemen, H.J.B. Dick, Focused melt flow and localized deformation in the upper mantle: Juxtaposition of replacive dunite and ductile shear zones in the Josephine peridotite, SW Oregon, J. Geophys. Res. 100 (1995) 423–438.

[4] E. Aharonov, J. Whitehead, P.B. Kelemen, M. Spiegelman, Channeling instability of upwelling melt in the mantle, J. Geophys. Res. 100 (1995) 20433–20450.

[5] M. Spiegelman, P.B. Kelemen, E. Aharonov, Causes and consequences of flow organization during melt transport: the reactive infiltration instability in compactible media, J. Geophys. Res. 106 (2001) 2061–2077.

[6] Y. Liang, Y. Guo, Reactive dissolution instability driven by chemical diffusion with applications to harzburgite reactive dissolution, Geophys. Res. Lett., 30(2003)10.1029/2003GL017687.

[7] S.J. Lippard, A.W. Shelton, I.G. Gass, The Ophiolite of Northern Oman, Blackwell Scientific Publishing, Oxford, 1986, 178 pp.

[8] G. Suhr, H.A. Seck, N. Shimizu, D. Gunther, G. Jenner, Infiltration of refractory melts into the lowermost oceanic crust: evidence from dunite- and gabbro-hosted clinopyroxenes in the Bay of Islands ophiolite, Contrib. Mineral. Petrol. 131 (1998) 136–154.

[9] K. Kubo, Dunite formation processes in highly depleted peridotite: Case study of the Iwanaidake peridotite, Hokkaido, Japan, J. Petrol. 43 (2002) 423–448.

[10] J.E. Quick, The origin and significance of large, tabular dunite bodies in the Trinity peridotite, Northern California, Contrib. Mineral. Petrol. 78 (1981) 413–422.

[11] N. Takahashi, Evidence for melt segregation towards fractures in the Horoman mantle peridotite complex, Nature 359 (1992) 52–55.

[12] V.G. Batanova, A.V. Sobolev, Compositional heterogeneity in subduction-related mantle peridotites, Troodos massif, Cyprus, Geology 28 (2000) 55–58.

[13] P.B. Kelemen, Reaction between ultramafic rock and fractionating basaltic magma I. Phase relations, the origin of calc-alkaline magma series, and the formation of discordant dunite, J. Petrol. 31 (1990) 51–98.

[14] P.D. Asimow, E.M. Stolper, Steady-state mantle-melt interactions in one dimension: I. Equilibrium transport and melt focusing, J. Petrol. 40 (1999) 475–494.

[15] M.S. Ghiorso, R.O. Sack, Chemical mass transfer in magmatic processes IV. A revised and internally consistent thermodynamic model for the interpolation and extrapolation of liquid-solid equilibria in magmatic systems at elevated temperatures and pressures, Contrib. Mineral. Petrol. 119 (1995) 197–212.

[16] G. Suhr, E. Hellebrand, J.E. Snow, H.A. Seck, A.W. Hofmann, Significance of large, refractory dunite bodies in the upper mantle of the Bay of Islands ophiolite, Geochem. Geophys. Geosyst. 4 (2003) 10.1029/2001GC000277.

[17] P.C. Lichtner, Continuum formulation of multicomponent-multiphase reactive transport, in: P.C. Lichtner, C.I. Steefel, E.H. Oelkers (Eds.), Reactive Transport in Porous Media, Mineral. Soc. Am. 34, 1996, pp. 1–81.

[18] L.-C. Kuo, R.J. Kirkpatrick, Kinetics of crystal dissolution in the system diopside-forsterite-silica, Am. J. Sci. 285 (1985) 51–90.

[19] L.-C. Kuo, R.J. Kirkpatrick, Dissolution of mafic minerals and its implications for the ascent velocities of peridotite-bearing basalt magmas, J. Geol. 93 (1985) 691–700.

[20] C.H. Donaldson, The rates of dissolution of olivine, plagioclase, and quartz in a basalt melt, Mineral. Mag. 49 (1985) 683–693.

[21] M. Brearley, C.M. Scarfe, Dissolution rates of upper mantle minerals in an alkali basalt melt at high pressure: An experimental study and implications for ultramafic xenolith survival, J. Petrol. 27 (1986) 1157–1182.

[22] Y. Zhang, D. Walker, C.E. Lesher, Diffusive crystal dissolution, Contrib. Mineral. Petrol. 102 (1989) 492–513.

[23] C.S.J. Shaw, Y. Thibault, A.D. Edgar, F.E. Lloyd, Mech-

anisms of orthopyroxene dissolution in silica-undersaturated melts at 1 atmosphere and implications for the origin of silica-rich glass in mantle xenoliths, Contrib. Mineral. Petrol. 132 (1998) 354–370.
[24] C.S.J. Shaw, Dissolution of orthopyroxene in basanitic magma between 0.4 and 2 GPa: further implications for the origin of Si-rich alkaline glass inclusions in mantle xenoliths, Contrib. Mineral. Petrol. 135 (1999) 114–132.
[25] M.R. Fisk, Basalt magma interaction with harzburgite and the formation of high-magnesium andesites, Geophys. Res. Lett. 13 (1986) 467–470.
[26] C.C. Lundstrom, Rapid diffusive infiltration of sodium into partially molten peridotite, Nature 403 (2000) 527–530.
[27] P.B. Kelemen, D.B. Joyce, J.D. Webster, J.R. Holloway, Reaction between ultramafic rock and fractionating basaltic magma; II. Experimental investigation of reaction between olivine tholeiite and harzburgite at 1150–1050°C and 5 kb, J. Petrol. 31 (1990) 99–134.
[28] M.J. Daines, D.L. Kohlstedt, The transition from porous to channelized flow due to melt/rock reaction during melt migration, Geophys. Res. Lett. 21 (1994) 145–148.
[29] Y. Liang, Dissolution in molten silicates: Effects of solid solution, Geochim. Cosmochim. Acta 64 (2000) 1617–1627.
[30] Y. Liang, Kinetics of crystal-melt reaction in partially molten silicates: I. Grain scale processes, Geochem. Geophys. Geosyst. 4 10.1029/2002GC000375.
[31] Y. Liang, D. Elthon, Geochemistry and petrology of spinel lherzolite xenoliths from Xalapasco de La Joya, San Luis Potosi, Mexico: Partial melting and mantle metasomatism, J. Geophys. Res. 95 (1990) 15859–15877.
[32] Y. Liang, Diffusive dissolution in ternary systems: analysis with applications to quartz and quartzite dissolution in molten silicates, Geochim. Cosmochim. Acta 63 (1999) 3983–3995.
[33] J.C. Ayers, J.B. Brenan, E.B. Watson, D.A. Wark, W.G. Minarik, A new capsule technique for hydrothermal experiments using the piston-cylinder apparatus, Am. Mineral. 77 (1992) 1080–1086.
[34] E.B. Watson, D.A. Wark, J.D. Price, J.A. VanOrman, Mapping the thermal structure of solid-media pressure assemblies, Contrib. Mineral. Petrol. 142 (2002) 640–652.
[35] E.E. Underwood, Quantitative Stereology, Addison-Wesley, Reading, MA, 1970, 274 pp.
[36] E.B. Watson, D.R. Baker, Chemical diffusion in magmas: an overview of experimental results and geochemical applications, in: L.L. Perchuk, I. Kushiro (Eds.), Physical Chemistry of Magmas, Springer, New York, 1991, pp. 120–151.
[37] Y. Liang, F.M. Richter, E.B. Watson, Diffusion in silicate melts: II. Multicomponent diffusion in CaO-Al_2O_3-SiO_2 at 1500°C and 1 GPa, Geochim. Cosmochim. Acta 60 (1996) 5021–5035.
[38] F.M. Richter, Y. Liang, W.G. Minarik, Multicomponent diffusion and convection in molten MgO-Al_2O_3-SiO_2, Geochim. Cosmochim. Acta 62 (1998) 1985–1991.
[39] Z.T. Morgan, Y. Liang, An experimental study of orthopyroxene and harzburgite reactive dissolution in a basaltic-andesite melt, EOS Suppl. 81 (2000) F1292.
[40] M. Ito, H. Yurimoto, M. Morioka, H. Nagasawa, Co^{2+} and Ni^{2+} diffusion in olivine determined by secondary ion mass spectrometry, Phys. Chem. Miner. 26 (1999) 425–431.
[41] Y. Liang, A.M. Davis, Energetics of multicomponent diffusion in molten CaO-Al_2O_3-SiO_2, Geochim. Cosmochim. Acta 66 (2002) 635–646.
[42] C.E. Lesher, Kinetics of Sr and Nd exchange in silicate liquids: theory, experiments, and applications to uphill diffusion, isotopic equilibration, and irreversible mixing of magmas, J. Geophys. Res. 99 (1994) 9585–9604.
[43] D. McKenzie, The generation and compaction of partially molten rock, J. Petrol. 25 (1984) 713–765.
[44] W.D. Murray, F. Landis, Numerical and machine solutions of transient heat-conduction problems involving melting or freezing, Trans. ASME 81 (1959) 106–112.
[45] R.A. Tanzilli, R.W. Heckel, Numerical solutions to the finite, diffusion-controlled, two-phase, moving-interface problem (with planar, cylindrical, and spherical interfaces), Trans. Metal. Soc. AIME 242 (1968) 2313–2321.
[46] J. Crank, The Mathematics of Diffusion, Clarendon Press, Oxford, 1975, 414 pp.
[47] C.E. Ford, D.G. Russell, J.A. Craven, M.R. Fisk, Olivine-liquid equilibria: temperature, pressure and composition dependence of the crystal/liquid cation partition coefficients for Mg, Fe^{2+}, Ca and Mn, J. Petrol. 24 (1983) 256–265.
[48] S.R. Hart, K.E. Davis, Nickel partitioning between olivine and silicate melt, Earth Planet. Sci. Lett. 40 (1978) 203–219.
[49] P. Beattie, C. Ford, D. Russell, Partition coefficients for olivine-melt and orthopyroxene-melt systems, Contrib. Mineral. Petrol. 109 (1991) 212–224.
[50] R.O. Colson, D. Gust, Effects of pressure on partitioning of trace elements between low-Ca pyroxene and melt, Am. Mineral. 74 (1989) 31–36.
[51] P.B. Kelemen, S.R. Hart, S. Bernstein, Silica enrichment in the continental upper mantle via melt/rock reaction, Earth Planet. Sci. Lett. 164 (1998) 387–406.